

Original Research

Core Ideas

- We introduce a new geophysical imaging method to assess managed aquifer recharge sites.
- This method provides high-resolution 3D imaging of the subsurface down to a minimum depth of 50 m.
- We introduce Resistivity Distribution Plot as a new approach to assign a saturated–unsaturated boundary.

Assessment of Managed Aquifer Recharge Sites Using a New Geophysical Imaging Method

Ahmad A. Behroozmand,* Esben Auken, and Rosemary Knight

In many places around the world, much attention is focused on managed aquifer recharge (MAR) because of reduced groundwater levels due to droughts. To assess the suitability of a site for MAR, detailed three-dimensional (3D) information about the subsurface materials and their hydraulic properties is needed. In areas where the groundwater level is at an intermediate depth (e.g., 20–40 m), such information is needed from the ground surface down to a minimum depth of ~50 m. To achieve this goal, we used a new geophysical imaging system: a towed time-domain electromagnetic system that is efficient for acquiring data at a significantly improved resolution and a scale needed for MAR. During a 2-d period, we acquired ~92 line-kilometers of data in one almond [*Prunus dulcis* (Mill.) D.A. Webb] grove, one pistachio (*Pistacia vera* L.) grove, one open field, and two active recharge basins in the Tulare Irrigation District in the Central Valley of California. At each site, a detailed 3D resistivity model with a resolution down to the 10- by 10-m scale is presented in terms of resistivity distribution plots, which are then used to assign a saturated–unsaturated boundary. In addition, we used a resistivity–lithology transform to interpret the resistivity models and create lithology maps at each site. We used this information to assess the suitability of each site for MAR.

Abbreviations: 3D, three-dimensional; ATV, all-terrain vehicle; CVHM, Central Valley Hydrologic Model; DOI, depth of investigation; EM, electromagnetic; GPR, ground-penetrating radar; MAR, managed aquifer recharge; NMR, nuclear magnetic resonance; TEM, time-domain electromagnetic; tTEM, time-domain electromagnetic method towed behind an all-terrain vehicle.

Groundwater is a major source of water in California, making up 38% of the state's annual water supply in a wet year and up to 46% in a dry year. In some areas of California, groundwater is the only water supply. Periods of drought over the past 10 yr, with the shortage of surface water supplies, have led to extensive pumping of groundwater to meet irrigation needs. This has exacerbated the problem of groundwater depletion in many of the groundwater basins. Groundwater legislation passed in 2014, the Sustainable Groundwater Management Act, has made sustainable groundwater management a requirement in California, with many water agencies now developing groundwater sustainability plans to meet this requirement by 2020 or 2022. Of the various options available for reaching sustainability, much attention is now focused on managed recharge of the groundwater systems. There is a need for an improved understanding of the controls on managed aquifer recharge (MAR) and a need to find new approaches to enhance the volume of recharge.

The infiltration of water at the ground surface, which leads to the natural recharge of an aquifer, can occur over large discontinuous areas. The infiltration rates of the surface materials need to be sufficiently high to allow much of the water to infiltrate below the ground surface, as opposed to being removed through runoff or evaporation. With respect to the movement of water below the surface layer, the hydraulic conductivity of the underlying materials determines the path of the water and percolation rate, and the porosity determines the volume of storage. Identifying key areas on the ground surface contributing to MAR provides important input to land-use planning.

A.A. Behroozmand and R. Knight, Dep. of Geophysics, Stanford Univ., Stanford, CA 94305; E. Auken, HydroGeophysics Group, Dep. of Geoscience, Aarhus Univ., 8000 Aarhus C, Denmark. *Corresponding author (abehrooz@stanford.edu).

Received 4 Oct. 2018.
Accepted 18 Mar. 2019.

Citation: Behroozmand, A.A., E. Auken, and R. Knight. 2019. Assessment of managed aquifer recharge sites using a new geophysical imaging method. *Vadose Zone J.* 18:180184. doi:10.2136/vzj2018.10.0184

© 2019 The Author(s). This is an open access article distributed under the CC BY-NC-ND license (<http://creativecommons.org/licenses/by-nc-nd/4.0/>).

Over the past 20 yr, there have been numerous projects throughout California where dedicated streams and ponds have been constructed and used for managed aquifer recharge (California Department of Water Resources, 2017; Luxem, 2017). A common approach is to capture storm water runoff during the winter months and to allow that water to infiltrate below the pond and later be recovered for use. In the past few years, growers in the Central Valley of California have been exploring the use of on-farm recharge, also referred to as “surface spreading,” where excess surface water in the winter months is used to flood fields or groves. As with MAR, when water is put into ponds, fields, or groves, the hydraulic properties of the surface/subsurface materials determine infiltration rates, the path of the water, and the volume of water that ultimately reaches and recharges the groundwater system. Therefore, when assessing the suitability of a site for an MAR pond or for on-farm recharge, information about the subsurface materials and their hydraulic properties is critical. Although poor infiltration leads to inefficiencies in a MAR pond, the consequences can be more serious when flooding groves or fields because ponding can damage trees or crops and increase the risk of disease.

The geology of the Central Valley of California is dominated by fine-grained materials with low hydraulic conductivity (K), with networks of high- K sand and gravel providing the pathways for recharge. Given the range of depths over which groundwater pumping has occurred, there is a desire to recharge both the shallow semi/unconfined aquifers and the deeper confined aquifers. Therefore, information is needed about lithology to assess the potential for shallow and/or deep MAR at a site. Soil maps are widely used to estimate the groundwater recharge suitability index (e.g., Soil Agricultural Groundwater Banking Index [O’Geen et al., 2015] or LandIQ [landiq.com]), but they do not provide information about the underlying material. Information about lithology to a depth of ~ 850 m can be obtained from the US Geological Survey’s groundwater model of the Central Valley, referred to as the Central Valley Hydrologic Model (CVHM) (Faunt, 2009). With a description of lithology, in this model described as percent of coarse-grained material, one can estimate hydraulic conductivity and model the recharge process. However, CVHM has spatial resolution on the order of ~ 1.6 km in the horizontal direction and ~ 15.2 m in the vertical direction. The density of selected well logs used in CVHM for the texture analysis was based on the quality of the driller’s log, meaning that the model uses either two higher-quality well logs when available or four lesser-quality well logs for a quarter township (~ 23.3 km²). Information can be obtained from drillers’ logs from wells in the area, or wells could be drilled or soil probes taken specifically to characterize a site of interest. None of these approaches is likely to provide the spatial resolution needed to model MAR.

A number of studies have shown the potential usefulness of geophysical methods to assess potential MAR sites. Various methods have been used, differing in terms of the area of coverage, depth of coverage, and spatial resolution; these methods are described below. The objective of this study was to evaluate a new geophysical

imaging method capable of providing the coverage and resolution that are optimal for the assessment of MAR sites in the Central Valley of California, where there is an interest in recharging both the shallow (<20 m) and intermediate (20–50 m) parts of the groundwater system. Over a 2-d period, we acquired data in one almond grove, one pistachio grove, one open field, and two active recharge basins in the Tulare Irrigation District in the central part of the San Joaquin Valley, California. We conclude that this new method, a time-domain electromagnetic (TEM) method towed behind an all-terrain vehicle (ATV) and called tTEM (Auken et al., 2018), is an efficient way to acquire the data needed to model MAR at a site and can advance our ability to identify important areas for natural recharge and inform the selection of sites for MAR or on-farm recharge. In this paper we define an “efficient” method as one that is suited for assessing MAR sites with respect to penetration depth and resolution and that can achieve maximum productivity with minimum cost and effort.

Background and Motivation

Among a wide variety of applications, surface geophysical methods have been used in MAR projects for improved understanding of the subsurface lithology (Ahmed et al., 2015; Maliva et al., 2015). The advantage of surface geophysical methods, compared with borehole methods, is that they allow denser and faster data coverage at a much lower cost. Different geophysical methods are sensitive to different physical parameters of the subsurface materials and have their own limitations with respect to the area of coverage, penetration depth, and spatial resolution.

Electrical resistivity (also called direct-current resistivity) and electromagnetic methods measure apparent electrical resistivity of the formation and have been used in MAR investigations to map the top soil, monitor infiltration, delineate the geometry of aquifers and variation in lithology, map the depth to the base of aquifers, locate boundaries between fresh and brackish water units, and develop models to simulate the flow and transport beneath a MAR pond (Abdalla et al., 2010; Behroozmand et al., 2017b; Berthold et al., 2004; Cook et al., 1992; Gottschalk et al., 2017; Lawrie et al., 2012; Mawer et al., 2016; Nenna et al., 2011; Parsekian et al., 2014; Pidlisecky and Knight, 2011). As an example, Mawer et al. (2016) used a combination of fiberoptic distributed temperature sensing and electrical resistivity tomography to characterize heterogeneity in infiltration rates during MAR. They found a strong relationship between electrical resistivity estimated from electrical resistivity tomography data and observed maximum infiltration rates and concluded that combining these two techniques can provide the information needed about the spatial variability in parameters controlling infiltration rates and thus improve the design and operation of an MAR pond.

Gravity methods measure changes in the local gravitational field of the Earth that are linked to changes in the mass and volume of water stored or withdrawn from the aquifers. Using this property, temporal-gravity methods have been used to monitor water level changes in unconfined aquifers during MAR and

groundwater withdrawal (Howle et al., 2002; Pool and Schmidt, 1997). As another application of the gravity methods, Chapman et al. (2008) conducted repeated gravity measurements before, during, and after infiltrations in an alluvial-fan aquifer in Utah. The data acquired in an array of gravity stations provided evidence of a groundwater mound formation during infiltration. In addition, the decline and migration of the gravity anomaly was used to track migration of infiltrated water at a specific direction. A fundamental limitation in the application of gravity methods for MAR is that they do not have the resolution needed to characterize subsurface heterogeneities.

The nuclear magnetic resonance (NMR) methods measure a response from water molecules that are stored in pores and provide information about water-filled porosity and pore size distributions (Behroozmand et al., 2015). Surface NMR has been used in groundwater studies to map the water table and structural variations within the aquifer (Behroozmand et al., 2017a; Chalikakis et al., 2008; Costabel et al., 2017). Additionally, surface NMR can be used during MAR to detect and characterize water in the unsaturated zone, as shown in a study by Walsh et al. (2014) at a managed aquifer storage and recovery facility in Arizona. However, its low coverage speed limits application of surface NMR for assessing MAR sites.

Surface ground-penetrating radar (GPR) methods use high-frequency electromagnetic signals to image the shallow subsurface by recording the reflected signals from the subsurface structures. Ground-penetrating radar surveys can be performed rapidly and provide high vertical and horizontal resolutions. Under favorable conditions, GPR can be used in groundwater recharge studies (Ferré et al., 2007; Strobach et al., 2010). However, an inherent limitation of GPR for most MAR applications is its shallow depth of investigation, especially in electrically conductive media.

Other studies include applications of combined geophysical methods in MAR (Affatato et al., 2014; Minsley et al., 2011). Finally, airborne electromagnetic (EM) methods have been used extensively for large-scale characterization of groundwater systems (Høyer et al., 2015; Knight et al., 2018; Pedersen et al., 2017). Typical airborne EM surveys comprise a relatively large line spacing (on the order of hundreds of meters) and high flight speed. Therefore, the estimated resistivity models can be used as an indicator of areas that are potential MAR sites and need finer-scale assessments. To make an airborne EM survey successful in detecting recharge areas, care should be taken when designing a survey, especially with respect to the airborne system, line spacing, flight speed, and bandwidth of the system (e.g., Asch et al., 2017). However, when it comes to assessing MAR sites, the size of the footprint of an airborne EM sounding is significantly larger than that of the τ TEM system used in this study. In addition, airborne EM methods are costly and are used for large-scale surveying; thus, they are less optimal for assessing MAR sites.

When studying a potential MAR site, especially in places like the Central Valley of California where the water table is at an intermediate depth level, it is important to use a method that is capable of characterizing both surface and subsurface materials in the unsaturated and saturated zones. Other important criteria include fast coverage, efficiency, and high resolution. Table 1 summarizes common surface geophysical methods used in studying MAR sites and highlights the pros and cons of each method with respect to penetration depth, resolution, coverage speed, and efficiency. The last row of the table describes the properties of the τ TEM system used in this study. We highlight that some structural features, like fractured soils or small karst features, may fall outside the resolution capabilities of τ TEM and need to be characterized using other methods. We did not include airborne EM methods in Table 1 because they are used

Table 1. Common surface geophysical methods used in studying managed aquifer recharge sites and pros and cons of each method with respect to penetration depth, resolution, coverage speed, and efficiency.

Method†	Hydrogeological objective	Penetration depth	Resolution	Coverage speed	Efficiency
Gravity	monitoring water level changes during managed aquifer recharge; tracking infiltrated water	NA‡	NA	low	inefficient
Surface NMR	detection and characterization of water in the unsaturated zone; tracking infiltrated water; mapping water table and structural variations	intermediate	high (vertical)/low (horizontal)	low	inefficient
GPR	mapping structural variations; imaging water table	shallow	high	medium/high	inefficient
Electrical resistivity	mapping structural variations; characterizing permeable and impermeable structures	intermediate	high	low	inefficient
FDEM	mapping structural variations; characterizing permeable and impermeable structures	too shallow	high, 3D§	low/high§	inefficient/efficient§
TEM	mapping structural variations; characterizing permeable and impermeable structures	deep	medium (vertical)/low (horizontal)	low	inefficient
τ TEM	mapping structural variations; characterizing permeable and impermeable structures; assessing recharge sites	intermediate	high, 3D	high	efficient

† FDEM, frequency-domain electromagnetic; GPR, ground-penetrating radar; NMR, nuclear magnetic resonance; TEM, time-domain electromagnetic; τ TEM, time-domain electromagnetic method towed behind an all-terrain vehicle.

‡ Not applicable.

§ Modern FDEM instruments and ground conductivity meters can be efficient and capable of fast coverage for shallow (<10-m) investigations (Christiansen et al., 2016).

for large-scale mapping and are not cost effective for assessing managed aquifer recharge sites.

Among the variety of geophysical methods, we have found that those that measure electrical resistivity are exceptionally suited to the MAR problem. The contrast in electrical resistivity between sands and gravels that are conductive to the flow of water and clays, which often act as barriers to flow, helps determine the suitability of the site for MAR (for a typical range of electrical resistivities of geological materials, see Fig. 2 in Palacky [1988]). However, until recently, no geophysical surveying system has existed that is appropriate for assessing MAR sites (i.e., a system that can map both shallow and intermediate depth intervals and is efficient and capable of a full three-dimensional [3D] imaging and fast coverage with high resolution). The new geophysical surveying system, τ TEM, is an ideally suited tool for assessing MAR sites because it fulfills the above-mentioned requirements. The system specifications are described below.

As a final step when working with methods that measure electrical resistivity, the relationship between resistivity and lithology can be used to transform resistivity models to lithologic models. Different approaches have been used to develop the resistivity–lithology transforms using lithologic logs and either colocated geophysical logs or the closest geophysical resistivity models. These approaches include establishing a transfer function between resistivity and the clay fraction (Foged et al., 2014), using artificial neural networks to build a transfer function between known electrical conductivity and geological parameters (Gunnink et al., 2012), and multiple-point statistics for stochastic hydrostratigraphic modeling (Barfod et al., 2018; Gottschalk et al., 2017). In this study, we used a resistivity–lithology transform that was developed in the study area between lithologic logs and closest airborne EM resistivity models (Knight et al., 2018), as discussed below.

◆ The Towed Time-Domain Electromagnetic System

The τ TEM system works based on the following physical principles. In short, a time-varying electrical current is ramped up in the transmitter loop and held at a steady state, which produces a static primary magnetic field, and is then abruptly turned off. When the transmitter current is abruptly turned off, the change in the primary magnetic field induces an electromotive force in the ground that results in electrical eddy currents in the subsurface. These eddy currents produce secondary magnetic fields, and, as time passes, the decaying secondary magnetic fields induce an electromotive force in the receiver coil. For a z -component receiver coil, the TEM signal is measured as time derivative of the vertical component of the magnetic field, B_z/dt . The signal ranges over a few orders of magnitude in a very short time period and contains the resistivity information of the subsurface. The early and late time data contain information of shallow and deep structures, respectively.

The idea of developing the τ TEM system was to make a system that provides high-resolution resistivity models in both

horizontal and vertical directions and images the subsurface down to a minimum depth of 40 m; however, given the right geology, the current τ TEM system is capable of imaging down to ~ 70 -m depth. Efficient 3D mapping of large areas was another important goal for developing τ TEM.

The τ TEM system uses a 2- by 4-m single-turn coil as a transmitter and a multi-turn 0.5- by 0.5-m coil with an effective area of 5 m² as a z -component receiver. The transmitter and receiver are separated by 9 m in an out-of-loop offset configuration. The electronic components are mounted on the back of an ATV, and the system is towed behind the ATV. The geographical position of the data is recorded continuously, and the navigation and data collection are controlled by the driver/operator. Typical operation speed is ~ 15 to 20 km h⁻¹. The τ TEM system is a dual-moment system using low and high moments to measure early and late time data that are used for shallow and deep investigations, respectively. Transmitter currents of ~ 2.8 and ~ 30 A are used for low- and high-moment data. All details about the τ TEM system specifications are presented by Auken et al. (2018).

◆ The Study Area

Our field sites are located in the Tulare Irrigation District, centrally located in the San Joaquin Valley of California. The District operates as a conjunctive use district, relying on surface water to meet irrigation needs and using groundwater when surface water is not available. Historically, imported water supplies were sufficient to meet the conjunctive use operations of the District. However, since the 1980s the District has seen a reduction in surface water supplies and a growing agricultural demand. This has resulted in a severe overdraft condition whereby growers are pumping more groundwater than is annually replenished to the aquifers. The District operates and maintains a system of recharge basins and is seeking new approaches to create a sustainable conjunctive use operation to comply with the Sustainable Groundwater Management Act. These new approaches include on-farm recharge without negatively affecting tree health or crop yields (i.e., where the geology of the farm is suitable for MAR). For this to be a viable option, an improved understanding of subsurface lithology distribution is needed for planning and operation of MAR projects.

◆ Data Acquisition and Derived Resistivity and Lithology Models

We conducted a 2-d field campaign in October 2017. The location of the field sites is shown in Fig. 1. The field sites consisted of two private properties where there is interest in on-farm recharge (one almond grove and one pistachio grove), one open field being considered as a new MAR basin, and two existing MAR basins. During this survey, the groves were last irrigated weeks before the τ TEM survey, the open field had no crops so there would have been no irrigation, and the two existing MAR basins had no water. Therefore, we expected minimal saturation differences in the shallow subsurface.

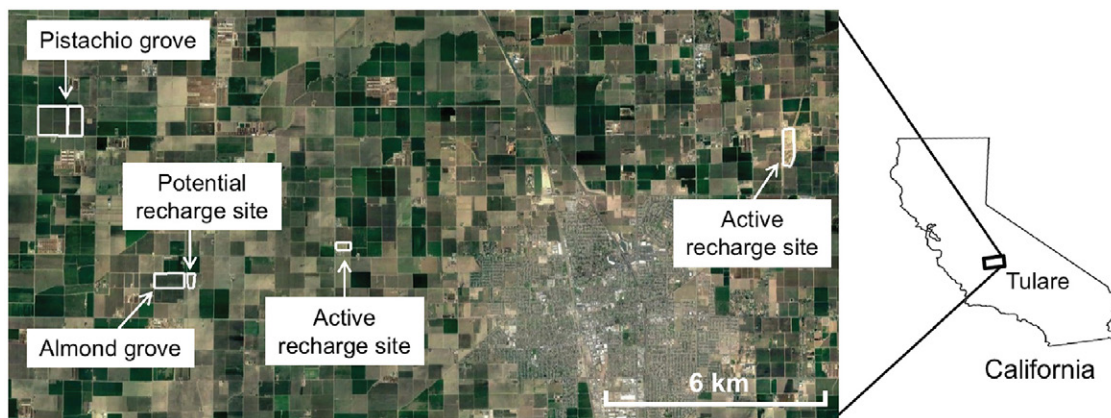


Fig. 1. Location map of the study sites in the Tulare Irrigation District, California. The base map is taken from Google Earth.

Site 1 is a 400- by 800-m almond grove. The private owner is considering on-farm recharge and has interest in learning about the lithology beneath the grove. The tTEM system, at ~ 2 m wide, fits perfectly between the rows of trees with their 6.8-m spacing (Fig. 2). We covered the entire grove in ~ 6 h, acquiring a total of 43 line-kilometers of data, with line spacing of 6.8 m. At this site, sounding data were acquired at every 2 to 2.5 m and were averaged during data processing, which led to datasets at every 10 to 12 m that were used for inversion (Auken et al., 2009). Figure 3a shows a 3D view of the resistivity model derived from the acquired data at Site 1. Warm colors (oranges and reds) correlate with high-resistivity units, and cool colors (blues) correlate with low-resistivity units. A base map (from Google Earth) is shown below the model to display the location of the acquired data. A total of 4359 inverted models, plotted next to each other in Fig. 3a, provide high-resolution 3D information of the subsurface.

Site 2 is an open field adjacent to the almond grove and is considered as a potential MAR site. At this site the data were acquired along six north-south lines with an average line spacing of 25 to 30 m and five east-west lines with an average line spacing of ~ 40 m, resulting in 2.8 line-kilometers of data. The data acquisition at Site 2 took ~ 30 min, with the ATV being driven at a lower speed due to the rough terrain. As a result, we acquired TEM soundings at every ~ 1 m, and the averaged data produced sounding spacings of 4 to 5 m, which were used for inversion. A 3D view of the resistivity model from the acquired data at this site is shown next to the data from Site 1 in Fig. 3a.

Site 3 is a 650- by 780-m pistachio grove and is also a candidate for on-farm recharge. Tree spacing at this site is 6 to 6.5

m. The system was driven between every third row of the trees; thus, the spacing between the lines is ~ 18 m. We acquired 30.1 line-kilometers data in ~ 4 h. The distances between the raw and averaged soundings at this site were ~ 2.5 m and 11 to 12 m, respectively. Figure 3b shows a 3D view of the resistivity model at this site.

Sites 4 through 7 are located at two of the district's existing MAR basins. Sites 4 and 5 are two cells of an active basin with a total area of 300 m by 1 km. We acquired 11.2 line-kilometers of data, with raw sounding spacings of 1 to 1.5 m and averaged data spacings of 6 to 7 m, which were used for inversion. The average line spacing was 15 to 20 m at Site 4 and 20 to 25 m at Site 5. The data acquisition at these two sites took ~ 3.5 h. Figure 3c shows a 3D view of the resistivity models of Sites 4 and 5. Similar to above, Sites 6 and 7 are two cells of an active basin and are 100 by 200 m and 200 by 280 m in size. A total of 4.8 line-kilometers of data was acquired at these two sites, with a line spacing of ~ 10 to 20 m and with a spacing of 2 to 2.5 m and 10 to 12 m between raw and averaged soundings, respectively. The data acquisition at Sites 6 and 7 took < 1 h. A 3D view of the resistivity model from the acquired data at Sites 6 and 7 is shown in Fig. 3d.

Overall, noise conditions were good at the study sites, and a good signal-to-noise ratio was obtained at each site. At each site, all acquired data were inverted together to obtain a model of electrical resistivity of the subsurface. The data processing and inversion were done using the Aarhus Workbench software (Aarhus GeoSoftware). We used a 30-layer smooth model and applied spatial constraints to the model parameters (Auken et al., 2015; Viezzoli et al., 2008). A multilayer model was chosen to better capture the complex geologic features at each site. The layer

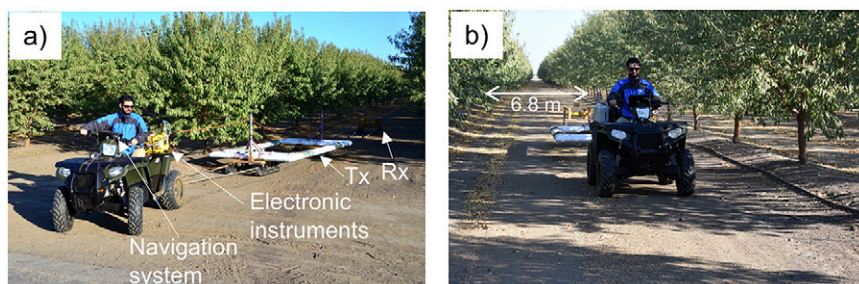


Fig. 2. Time-domain electromagnetic system towed behind an all-terrain vehicle in operation at Site 1 (almond grove). Tree spacing is 6.8 m.

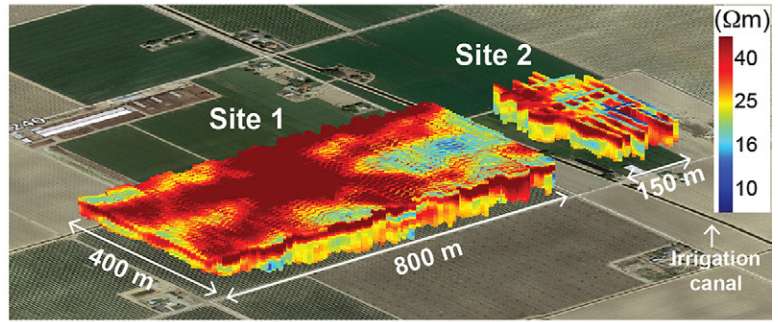
thickness started at 1 m at the top of each resistivity model and was increased by a factor of 1.1 down to the bottom of the model. During the inversion, the layer thicknesses were fixed, and vertical and horizontal constraints were used to impose correlation between neighboring model parameters. A 40Ω homogeneous half-space was used as a starting model, and no a priori constraints were used during the inversions. Following an approach presented by Christiansen and Auken (2012), the inverted models are displayed down to their depth of investigation (DOI) (i.e., an estimated depth below which the resolution of a model diminishes). This estimated depth is obtained by recalculating the Jacobian matrix of the final inverted model and application of a threshold value that indicates the minimum amount of sensitivity needed for indicative information.

Given the dense data coverage provided by t TEM, detailed 3D structural information is obtained at each site. In addition, we used resistivity distribution plots to evaluate the overall variations of lithology. The resistivity distribution plot of Site 1 is shown in Fig. 4a. This plot comprises all inverted resistivity models (here 4359) at the site and contains the following information:

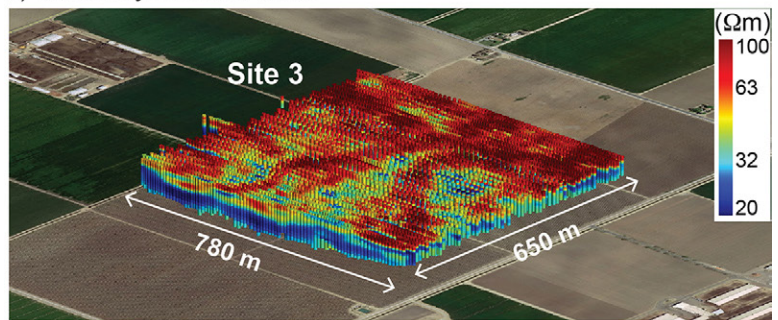
1. At each depth along the y axis, a distribution of resistivities for the entire site is plotted on a logarithmic scale. Examples of resistivity distributions at three depth intervals are shown in Fig. 4b. The shown location of the boundary between the unsaturated and saturated zone was determined through analysis of the distributions, described below. These plots show how the range and width of resistivity distributions vary as a function of depth.
2. At each resistivity value along the x axis, the color displays the number of models with that resistivity value. Therefore, warm colors indicate higher number of models with corresponding resistivity values.
3. Given a resistivity–lithology transform, corresponding ranges of resistivity values at each depth interval can be used to describe lithology, as discussed below.
4. Each resistivity model on the resistivity distribution plot is cut below its DOI. This, together with the number of models at each depth (i.e., the color of the distribution), provides, at the bottom part of each plot, information about the DOI at each site.

The ultimate goal when assessing a site for MAR is to identify the subsurface lithology. To do that, a resistivity–lithology transform is needed. In this study, we had a resistivity–lithology transform developed in the study area by Knight et al. (2018) (Fig. 5). The transform was built using airborne EM data and lithologic (drillers’) logs in the area. Each layer in the lithologic log had a described thickness and an assigned, simplified, lithology of either sand and gravel or clay within the unsaturated zone and of any sand and gravel, mixed fine and coarse, or clay within the saturated zone. To determine the resistivity values

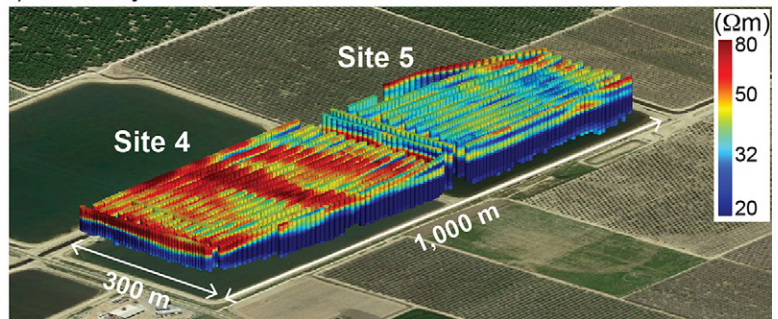
a) Resistivity models of Sites 1 & 2



b) Resistivity model of Site 3



c) Resistivity models of Sites 4 & 5



d) Resistivity models of Sites 6 & 7

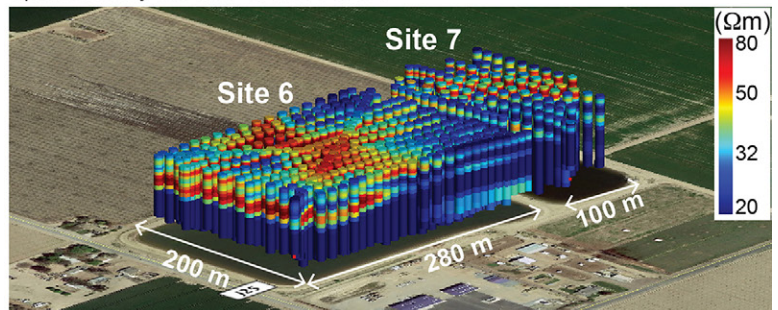


Fig. 3. Three-dimensional views of the resistivity models from the acquired data at Sites 1 through 7. Note the difference in the range of resistivity values among the sites.

corresponding to the lithologic units, the closest resistivity values to the lithology log, obtained through inversion of the airborne EM data, were used. Assuming that the electric field lines during the airborne EM measurement were parallel to the lithologic layering in the subsurface, the determined airborne EM resistivity values are mathematically related to the unknown resistivity values of the lithologic layers. A bootstrapping method was used to solve the system of equations, thereby obtaining a distribution of resistivity values for

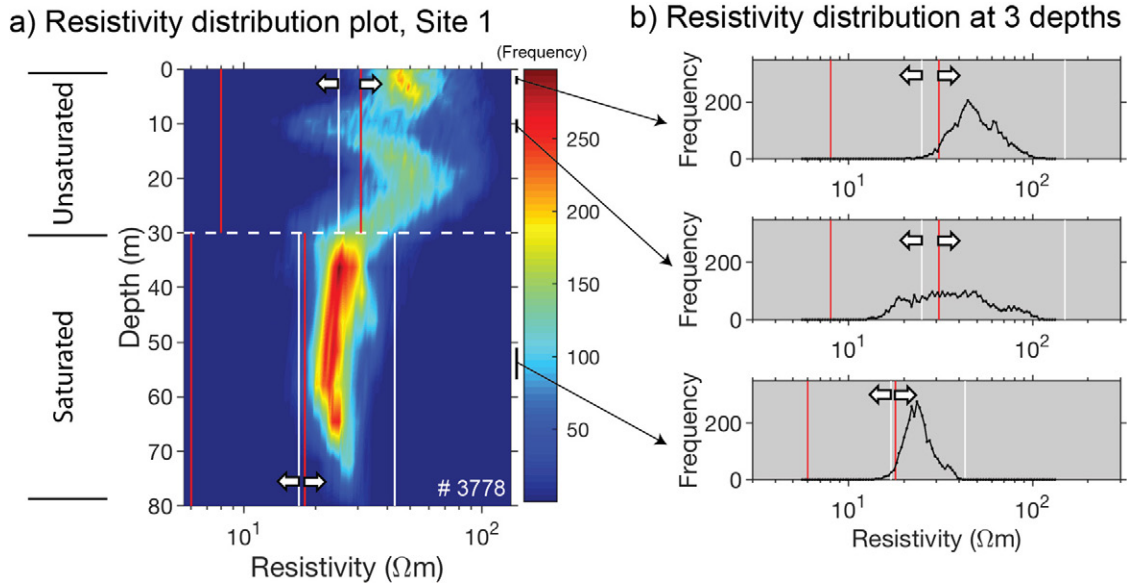


Fig. 4. (a) Resistivity distribution plot of Site 1: white dashed line shows the saturated–unsaturated boundary, red and white lines show clay and sand and gravel resistivity intervals obtained from the resistivity–lithology transform (note that different resistivity–lithology models are considered in the saturated and unsaturated zones), thick arrows indicate thresholds for clay and sand and gravel resistivity values, and the intervals between the thick arrows correspond to both clay and sand and gravel. The total number of inverted resistivity models at this site is shown at the bottom-right corner of the plot; and (b) examples of resistivity distributions at three depth intervals. Note the variation in the range and width of resistivity distributions.

each lithology type. This approach yielded one resistivity distribution for each lithology type for the unsaturated zone and one for the saturated zone, regardless of location or depth. This is a reasonable approach given the size of the study area ($\sim 100 \text{ km}^2$). A significant change in the distribution of resistivity values in the unsaturated and saturated zones was noted at the site due to the large impact of saturation on resistivity values, so separate transforms were built for unsaturated and saturated sediments. In addition, we assumed coarse-grained media and thus rapid saturation changes across the water table. In the unsaturated zone, it was found that clay resistivity values vary from 8 to 31 $\Omega \text{ m}$ (shown with red lines) and that sand and gravel resistivity values vary from 25 to 150 $\Omega \text{ m}$ (shown with white lines). We refer to these intervals as the clay resistivity interval and the sand and gravel resistivity interval. We highlight that resistivity of the clays in the unsaturated zone could also be sensitive to saturation because the clays can remain saturated for a longer period.

In the saturated zone, clay resistivity values vary from 6 to 18 $\Omega \text{ m}$ (shown with red lines), mixed fine and coarse resistivity values vary from 12 to 22 $\Omega \text{ m}$, and sand and gravel resistivity values vary from 17 to 43 $\Omega \text{ m}$ (shown with white lines). At our tTEM sites, we rarely observed layers with resistivity values corresponding to the interval where mixed fine and coarse are the most probable lithologic units in the saturated zone. Therefore, for the sake of simplicity we omitted the mixed fine and coarse classification from our interpretations. The thick arrows in Fig. 5 indicate thresholds for sand and gravel and clay resistivities. The resistivity intervals between the thick arrows, shown as hatched areas, correspond to clay and to sand and gravel and are referred to here as the overlapped resistivity interval.

We used this resistivity–lithology model to interpret our resistivity distribution plots but required information about the boundary between the saturated and unsaturated zone, given the impact of saturation on the resistivity transforms (Fig. 5).

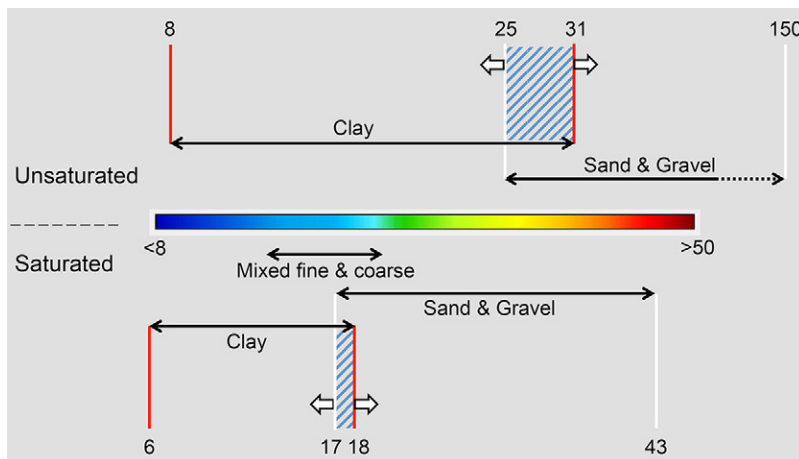


Fig. 5. A resistivity–lithology transform developed in the study area (Knight et al., 2018). Red and white lines show clay and sand and gravel resistivity intervals obtained from the resistivity–lithology transform. Note that different resistivity–lithology models are considered in the saturated and unsaturated zones. Thick arrows indicate thresholds for clay and sand and gravel resistivity values. The intervals between the thick arrows (hatched areas) correspond to both clay and sand and gravel. The color scale is similar to the one used by Knight et al. (2018).

Available water level data consist of California Department of Water Resources' groundwater level contour maps. However, the data used to create these maps are taken from wells, which are too sparse in our study area, with no well located at or close to our study sites. A similar problem was encountered with a "Fall 2017 Depth to Groundwater Map" from the Tulare Irrigation District, which is based on a more complete well database than the one of the Department of Water Resources. In addition, it was not clear whether groundwater level data were acquired in pumping wells or monitoring wells or when the data were acquired (during irrigation season or afterward). For these reasons, we did not find available water level data useful for this study. Therefore, we developed an approach that would allow us to use the resistivity distributions to identify the saturated–unsaturated boundary.

Our approach is based on two criteria:

1. Resistivity distribution collapse/broadening: When we consider the resistivity distribution plots, there is a collapse of the distribution (moving from top to bottom) or broadening of the distribution (moving from bottom to top) at a certain depth interval. This occurrence was used as a first indicator to define a saturated–unsaturated boundary, assuming that the groundwater table is parallel to the ground surface. Therefore, going from bottom to top, we picked an interval where the distribution broadening occurs on the resistivity distribution plot.
2. Magnitude of resistivity values: Following the resistivity–lithology model in Fig. 5, we plotted the saturated zone clay and sand and gravel resistivity intervals on top of the resistivity distribution plot, shown with red and white lines. Then we moved the saturated–unsaturated boundary (white dashed line) upward as long as there were no resistivity values greater than 43Ω , which is the upper limit for resistivity of sand and gravel in the saturated zone. When a saturated–unsaturated boundary is set, a different set of lines is plotted above the boundary to indicate clay and sand and gravel resistivity intervals in the unsaturated zone. Finally, we use these resistivity intervals to describe lithology.

To illustrate how these two criteria were used at each site, Fig. 6 shows resistivity distributions at three depth intervals above (Fig. 6a) and three depth intervals below (Fig. 6b) the saturated–unsaturated boundary at Site 1.

At Site 1, we observe a clear distribution broadening at a depth of ~ 30 m (Fig. 4a). We also observe that resistivity values $>43 \Omega$ m only occur above this depth. Therefore, this depth is considered to be the saturated–unsaturated boundary. In the saturated zone, nearly all resistivity values are larger than the sand and gravel threshold (shown with a thick arrow), which indicates coarse-grained sediments in the aquifer down to the DOI. Similarly, most resistivity values in the unsaturated zone are interpreted as sand and gravel. We observe a layer with a broad resistivity distribution at a depth interval of 8 to 12 m with values corresponding to clay and to sand and gravel sediments. With respect to MAR, we conclude that this layer does not act as a hydraulic barrier. Most of the resistivity values in this layer correspond with sand and gravel. In addition, we see on a mean resistivity plan view map at this

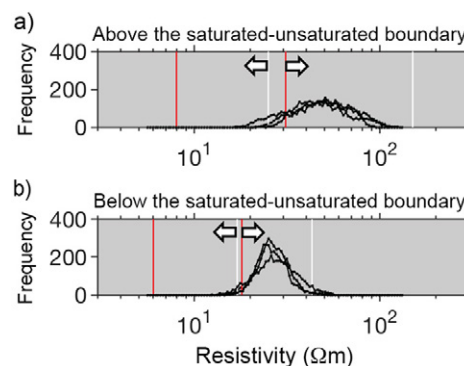


Fig. 6. Examples of resistivity distributions at three depth intervals above (a) and three depth intervals below (b) the saturated–unsaturated boundary at Site 1. Note the variation in the range and width of resistivity distributions above and below the saturated–unsaturated boundary. Red and white lines show clay and sand and gravel resistivity intervals obtained from the resistivity–lithology transform. Note that different resistivity–lithology models are considered in the saturated and unsaturated zones. Thick arrows indicate thresholds for clay, sand and gravel resistivity values. The intervals between the thick arrows correspond to both clay and sand and gravel.

depth interval that the clays are localized in a small portion of the site (Fig. 7a). Figure 7b shows a similar map that is color coded as sand and gravel resistivity intervals (yellow), overlapped resistivity intervals (green), and clay resistivity intervals (blue), following the resistivity interval values in Fig. 5.

With this information, we conclude that Site 1 is a good candidate for on-farm recharge and that water is expected to infiltrate easily through the coarse sediments in the unsaturated zone.

The resistivity distribution plots from Sites 2 to 7 are shown in Fig. 8. This figure shows how the resistivity structures vary between the study sites. We used the same approach as above to interpret the resistivity distribution plots to assess the suitability of each site for MAR. At Site 2, located close to Site 1 as shown in Fig. 3a, a saturated–unsaturated boundary is set at a depth of ~ 25 m. Similar to Site 1, saturated zone sediments at this site are interpreted as sand and gravel but with a broader resistivity distributions compared with the saturated zone resistivity distributions at Site 1, indicating a more heterogeneous aquifer at this site. In the unsaturated zone, however, smaller resistivity values are observed in the top ~ 15 m, with most of the values interpreted as mixed clay and sand and gravel sediments. We observe a low-resistivity layer at a depth of ~ 5 to 12 m, with most of the sediments interpreted as clay, meaning that this layer is not conductive to the flow of water. Therefore, we concluded that Site 2 may not be appropriate for MAR because the top ~ 15 m of the unsaturated zone is dominated by fine-grained sediments. An example of resistivity and lithology sections from Site 2 is given below.

At Site 3 (the pistachio grove), a saturated–unsaturated boundary is placed at a depth of 29 m (Fig. 8b). In the saturated zone, the resistivity values are interpreted as sand and gravel for the entire zone down to the DOI. Compared with the resistivity structures at Sites 1 and 2, a change in the magnitude of the resistivities

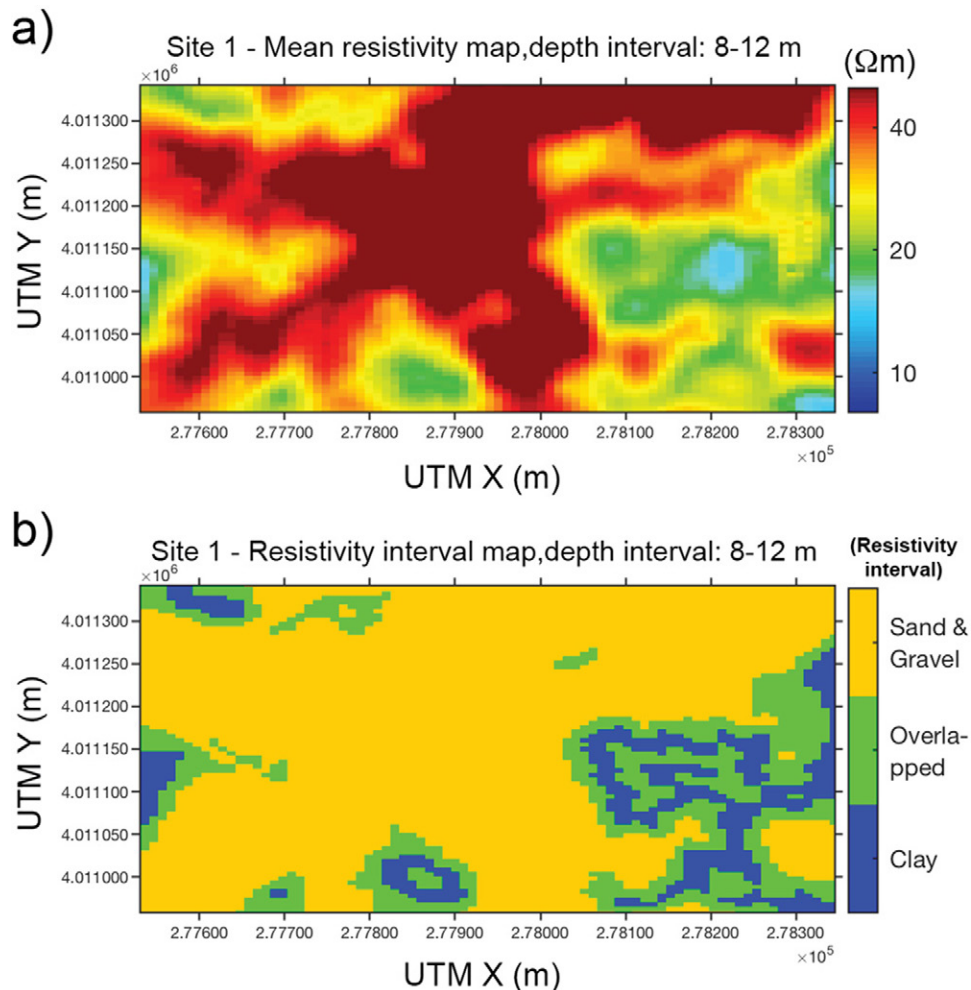


Fig. 7. (a) A plan view map showing mean resistivity values at depth interval of 8 to 12 m at Site 1, and (b) a similar map showing color-coded sand and gravel resistivity intervals (yellow), overlapped resistivity intervals (green), and clay resistivity intervals (blue), following the values in Fig. 5. For this depth interval, it is observed that most of the resistivity values throughout the site correspond to sand and gravel and therefore this layer does not act as a hydraulic barrier for MAR.

within the saturated zone can be interpreted as internal lithologic variations in depth. Above the saturation level, the resistivity structure suggests sand and gravel sediments, with a small proportion of mixed sediments from ~ 15 to 29 m. The resistivity structure of Site 3 suggests that this site is an appropriate site for MAR because the unsaturated zone consists mainly of coarse-grained sediments.

At Site 4, we placed a saturated–unsaturated boundary at a depth of 27 m (Fig. 8c). The saturated zone sediments have lower resistivity values than those at Sites 1 to 3. Assuming a fresh water aquifer in the area, this lower range of resistivities suggests finer-grain sediments in the aquifer. In the unsaturated zone, most of the resistivity values are in the sand and gravel resistivity interval, and a small proportion of the values fall in the overlapped resistivity interval. With these results, we conclude that Site 4 is also appropriate for MAR.

Site 5 is located close to Site 4. At this site, the saturated zone sediments have higher resistivity values than the corresponding values at Site 4 (Fig. 8d). The saturated zone sediments are described mainly as sand and gravel. Above the saturated–unsaturated

boundary, placed at a depth of 27 m, most of the resistivity values are in the sand and gravel range. At a depth of ~ 10 m, we observe a lower-resistivity layer, with resistivity values mainly in the overlapped resistivity interval. A plan view map of mean resistivity values at depth interval 9 to 11 m is shown in Fig. 9a. Figure 9b shows a similar map that is color coded as sand and gravel resistivity intervals (yellow), overlapped resistivity intervals (green), and clay resistivity intervals (blue), following the values in Fig. 5. These maps show that sediments with resistivity values corresponding with the clay resistivity interval and the overlapped resistivity interval (i.e., either clay or sand and gravel) are spread across Site 5, mostly on the western part. The possible presence of clay is not highly favored for MAR. However, we observe that high-resistivity values form a channel on the western part of the map, crossing the map from west to east, and extend into the eastern part of the map. This high-resistivity channel can act as a preferential infiltration path for water on the western part of the site. Based on these results, Site 5 may also be considered an appropriate site for MAR

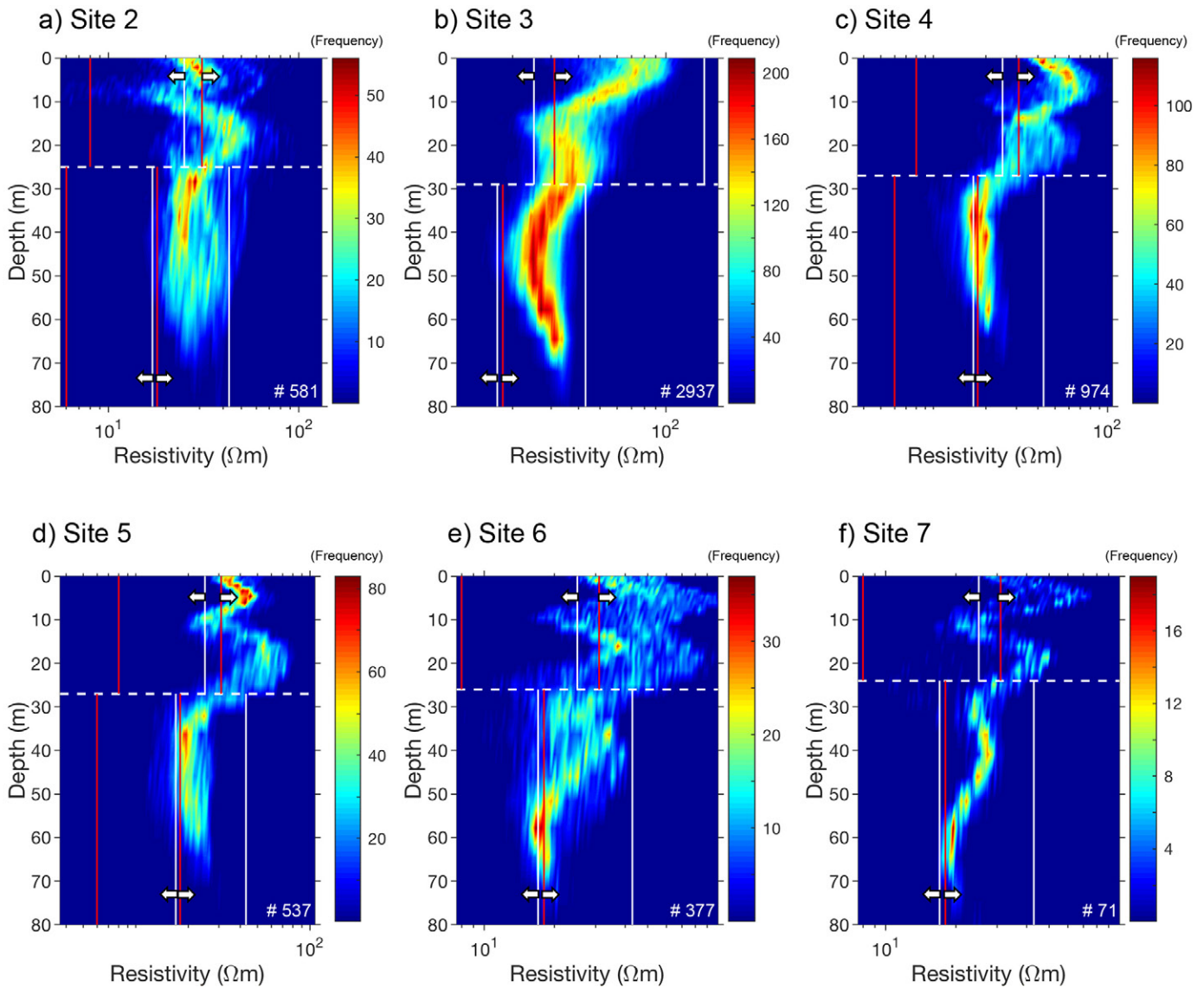


Fig. 8. Resistivity distribution plots from Sites 2 through 7. In each plot, the white dashed line shows the saturated–unsaturated boundary. Red and white lines show clay and sand and gravel resistivity intervals obtained from the resistivity–lithology transform. Note that different resistivity–lithology models are considered in the saturated and unsaturated zones. Thick arrows indicate thresholds for clay sand and gravel resistivity values. The intervals between the thick arrows correspond to both clay and sand and gravel. The total number of inverted resistivity models at each site is shown at the bottom-right corner of the plots.

because most of the unsaturated zone is comprised of sand and gravel sediments and because the lower-resistivity layer at 10 m depth will not act as a hydraulic barrier to MAR.

The resistivity structure at Site 6 looks different from those of the other study sites (Fig. 8e). With the exception of the bottom part of the saturated zone, we observe broad resistivity distributions over the entire depth range, which indicates geologic variation. In the upper part of the saturated zone, the resistivity values are mainly in the sand and gravel resistivity interval. A structural variation is observed from ~ 48 m to the DOI, with resistivity values being interpreted mainly as clay or mixed clay and sand and gravel sediments. Above the saturated–unsaturated boundary at 26 m, most of the resistivity values are in the sand and gravel resistivity interval. In a layer at a depth

of ~ 10 m, a small proportion of the resistivity values are in the clay resistivity interval. However, because most of the resistivity values in this layer are in the sand and gravel resistivity interval, this layer is not expected to act as a hydraulic barrier. Therefore, we conclude, based on the resistivity results, that Site 6 is a good candidate for MAR.

At Site 7, a saturated–unsaturated boundary was placed at a depth of 24 m (Fig. 8f). Nearly all resistivity values in the saturated zone are interpreted as sand and gravel sediments. At this site, we also observe resistivity variations within the saturated zone, with lower resistivity values at the bottom of the zone. The unsaturated zone consists of sand and gravel sediments, except for a low-resistivity layer centered at a depth of 10 m. The resistivity values in this layer are mainly in the clay and overlapped resistivity

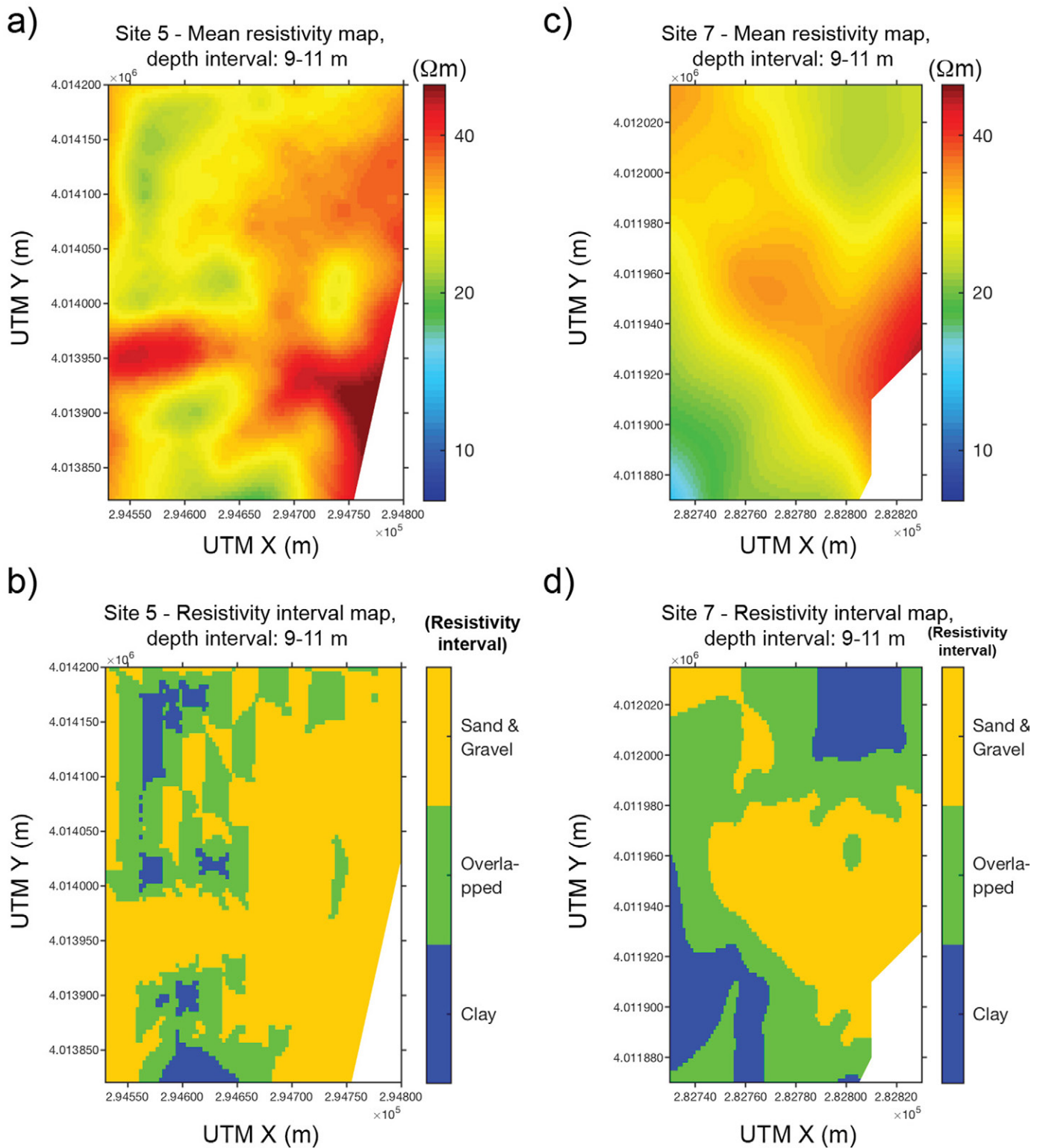
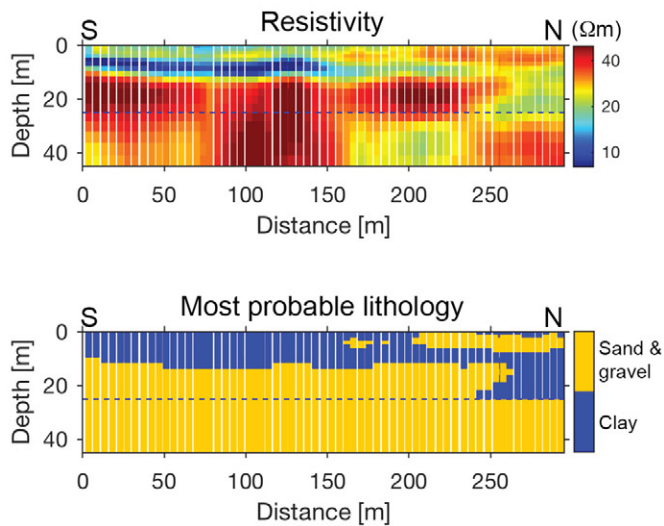


Fig. 9. Plan view maps showing mean resistivity values at depth interval 9 to 11 m at (a) Site 5 and (c) Site 7; similar maps showing color-coded sand and gravel resistivity intervals (yellow), overlapped resistivity intervals (green), and clay resistivity intervals (blue) at (b) Site 5 and (d) Site 7, following the values in Fig. 5.

intervals. Looking at plan view maps of mean resistivities and resistivity intervals in the depth interval of 9 to 11 m (Fig. 9c and 9d), we observe in most places resistivity values that correspond with clay or mixed clay and sand and gravel sediments. In addition, the

sand and gravel resistivity intervals are not continuous across the site. Based on the above information, we conclude that Site 7 may not be well suited for MAR. An example of resistivity and lithology sections from this site is given below.

a) Site 2



b) Site 7

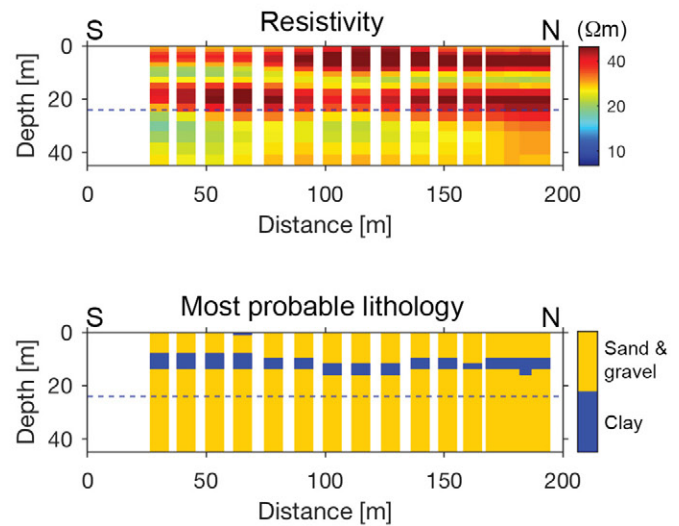


Fig. 10. Resistivity (Row 1) and most probable lithology (Row 2) distributions along two representative north-south profiles at (a) Site 2 and (b) Site 7. Blue dashed lines on each plot represent a saturated–unsaturated boundary obtained from the results in Fig. 8.

Deriving Lithologic Maps

The resistivity histograms obtained from the resistivity–lithology models of saturated and unsaturated zones consist of two intervals of resistivity values that can be interpreted, with a high degree of confidence, as 100% clay or 100% sand and gravel, and an overlap interval for which resistivity values can be interpreted as either clay or sand and gravel. This information can be used to create probability maps for different lithologic units. In addition, the resistivity distributions from the resistivity–lithology model can be used to create maps of the most probable lithologic unit at each site. The results along two representative profiles at Sites 2 and 7 are shown in Fig. 10. Row 1 shows resistivity sections sliced through the 3D models along two north-south profiles at Sites 2 and 7, and Row 2 shows the corresponding most probable lithology sections, with yellow and blue colors indicating sand and gravel and clay sediments, respectively. A blue dashed line in each panel represents the saturated–unsaturated boundary obtained from interpretation of the resistivity distribution plots at each site and is used to separate the two resistivity–lithology models. Following our discussion above, the most probable lithology sections in Fig. 10 show the presence of continuous clay layers in the unsaturated zone at Sites 2 and 7, which again suggests that these two sites may not be appropriate for MAR.

Conclusions

We used a new geophysical imaging system, τ TEM, to assess the suitability of MAR sites in the Central Valley of California. The τ TEM system is perfectly suited for studying MAR sites because it is efficient and provides a high-resolution 3D image of the subsurface down to a depth of >60 m, mapping out both unsaturated and saturated zones even in places where the groundwater level is relatively deep. The results of our 2-d survey provided detailed resistivity models at seven study sites. The resistivity distribution plots

were used to assign a saturated–unsaturated boundary at each site, allowing us to then use resistivity–lithology transforms to interpret the resistivity models in terms of lithology. The results of our study suggest that five of the seven sites are appropriate for MAR.

Acknowledgments

This project was funded by Stanford School of Earth, Energy and Environmental Sciences and by the Center for Groundwater Evaluation and Management in the Stanford Geophysics Department (gemcenter.stanford.edu). We thank Aaron Fukuda of Tulare Irrigation District for great help that facilitated this research project; the landowners for access to their property; Meredith Goebel, Stanford University, for help in the field; and Pradip Kumar Maurya and Jesper Pedersen, Aarhus University, for online quality control of the field data.

References

- Abdalla, O.A.E., M. Ali, K. Al-Higgi, H. Al-Zidi, I. El-Hussain, and S. Al-Hinai. 2010. Rate of seawater intrusion estimated by geophysical methods in an arid area: Al Khabourah, Oman. *Hydrogeol. J.* 18:1437–1445. doi:10.1007/s10040-010-0606-0
- Affatato, A., F. Accaino, and L. Baradello. 2014. Geophysical methods as support to aquifer recharge. *Procedia Eng.* 89:1249–1253. doi:10.1016/j.proeng.2014.11.428
- Ahmed, S., T. Arora, S. Sarah, F.A. Dar, T.K. Gaur, and P. Raghuvendar. 2015. Viewing sub-surface for an effective managed aquifer recharge from a geophysical perspective. In: T. Wintgens et al., editors, *Natural water treatment systems for safe and sustainable water supply in the Indian context*. IWA Publ., London. p. 301–315.
- Asch, T.H., J.D. Abraham, and J.C. Cannia. 2017. AEM-based hydrogeological frameworks in the Owens and Central Valleys of California. *Fast Times* 22(3):47–56.
- Auken, E., A.V. Christiansen, C. Kirkegaard, G. Fiandaca, C. Schamper, A.A. Behroozmand, et al. 2015. An overview of a highly versatile forward and stable inverse algorithm for airborne, ground-based and borehole electromagnetic and electric data. *Explor. Geophys.* 46:223–235. doi:10.1071/EG13097
- Auken, E., A. Christiansen, J. Westergaard, C. Kirkegaard, N. Foged, and A. Viezzoli. 2009. An integrated processing scheme for high-resolution airborne electromagnetic surveys, the SkyTEM system. *Explor. Geophys.* 40:184–192. doi:10.1071/EG08128

- Auken, E., N. Foged, J. Larsen, K. Lassen, P. Maurya, S.M. Dath, and T.T. Eiskjær. 2018. tTEM: A towed TEM-system for detailed 3D imaging of the top 70 meters of the subsurface. *Geophysics* 84(1). doi:10.1190/geo2018-0355.1
- Barfod, A.A.S., I. Møller, A.V. Christiansen, A.-S. Høyer, J. Hoffmann, J. Straubhaar, et al. 2018. Hydrostratigraphic modeling using multiple-point statistics and airborne transient electromagnetic methods. *Hydrol. Earth Syst. Sci.* 22:3351–3373. doi:10.5194/hess-22-3351-2018
- Behroozmand, A.A., K. Keating, and E. Auken. 2015. A review of the principles and applications of the NMR technique for near-surface characterization. *Surv. Geophys.* 36:27–85. doi:10.1007/s10712-014-9304-0
- Behroozmand, A.A., R. Knight, M. Müller-Petke, E. Auken, A.A.S. Barfod, T.P.A. Ferré, et al. 2017a. Successful sampling strategy advances laboratory studies of NMR logging in unconsolidated aquifers. *Geophys. Res. Lett.* 44:11021–11029. doi:10.1002/2017GL074999.
- Behroozmand, A.A., P. Teatini, J.B. Pedersen, E. Auken, O. Tosatto, A. Vest Christiansen. 2017b. Anthropogenic wetlands due to over-irrigation of desert areas: A challenging hydrogeological investigation with extensive geophysical input from TEM and MRS measurements. *Hydrol. Earth Syst. Sci.* 21:1527–1545. doi:10.5194/hess-21-1527-2017
- Berthold, S., L.R. Bentley, and H. Masaki. 2004. Integrated hydrogeological and geophysical study of depression-focused groundwater recharge in the Canadian prairies. *Water Resour. Res.* 40:W06505. doi:10.1029/2003WR002982
- California Department of Water Resources. 2017. Flood MAR: Using flood water for managed aquifer recharge to support sustainable water resources. California Dep. Water Res., Sacramento.
- Chalikakis, K., M.R. Nielsen, and A. Legchenko. 2008. MRS applicability for a study of glacial sedimentary aquifers in Central Jutland, Denmark. *J. Appl. Geophys.* 66:176–187. doi:10.1016/j.jappgeo.2007.11.005
- Chapman, D., E. Sahm, and P. Gettings. 2008. Monitoring aquifer recharge using repeated high-precision gravity measurements: A pilot study in South Weber, Utah. *Geophysics* 73:WA83–WA93. doi:10.1190/1.2992507
- Christiansen, A., and E. Auken. 2012. A global measure for depth of investigation. *Geophysics* 77(4):WB171–WB177. doi:10.1190/geo2011-0393.1
- Christiansen, A.V., J.B. Pedersen, E. Auken, N.E. Søre, M.K. Holst, and S.M. Kristiansen. 2016. Improved geoaerological mapping with electromagnetic induction instruments from dedicated processing and inversion. *Remote Sens.* 8(12):1022. doi:10.3390/rs8121022
- Cook, P.G., G.R. Walker, G. Buselli, I. Potts, and A.R. Dodds. 1992. The application of electromagnetic techniques to groundwater recharge investigations. *J. Hydrol.* 130:201–229. doi:10.1016/0022-1694(92)90111-8
- Costabel, S., B. Siemon, G. Houben, and T. Günther. 2017. Geophysical investigation of a freshwater lens on the island of Langeoog, Germany: Insights from combined HEM, TEM and MRS data. *J. Appl. Geophys.* 136:231–245. doi:10.1016/j.jappgeo.2016.11.007
- Faunt, C.C., editor. 2009. Groundwater availability of the Central Valley Aquifer, California. Prof. Pap. 1766. USGS, Reston, VA. doi:10.3133/pp1766
- Ferré, T.P.A., A.M. Binley, K.W. Blasch, J.B. Callegary, S.M. Crawford, J.B. Fink, et al. 2007. Geophysical methods for investigating ground-water recharge. Prof. Pap. 1703, Appendix 2. USGS, Reston, VA.
- Foged, N., P.A. Marker, A.V. Christiansen, P. Bauer-Gottwein, F. Jørgensen, A.-S. Høyer, et al. 2014. Large-scale 3-D modeling by integration of resistivity models and borehole data through inversion. *Hydrol. Earth Syst. Sci.* 18:4349–4362. doi:10.5194/hess-18-4349-2014
- Gottschalk, I.P., T. Hermans, R. Knight, J. Caers, D.A. Cameron, J. Regnerye, et al. 2017. Integrating non-colocated well and geophysical data to capture subsurface heterogeneity at an aquifer recharge and recovery site. *J. Hydrol.* 555:407–419. doi:10.1016/j.jhydrol.2017.10.028
- Gunnink, J.L., J.H.A. Bosch, B. Siemon, B. Roth, and E. Auken. 2012. Combining ground-based and airborne EM through Artificial Neural Networks for modelling glacial till under saline groundwater conditions. *Hydrol. Earth Syst. Sci.* 16:3061–3074. doi:10.5194/hess-16-3061-2012
- Howle, J.F., S.P. Phillips, M.E. Ikehara, and P.J. Dillon. 2002. Estimating water-table change using microgravity surveys during an ASR program in Lancaster, California. In: P.J. Dillon, editor, *Management of aquifer recharge for sustainability: Proceedings of the 4th International Symposium on Artificial Recharge of Groundwater, ISAR-4, Adelaide, SA, Australia.* 22–26 Sept. 2002. CRC Press, Boca Raton, FL. p. 269–272.
- Høyer, A.-S., F. Jørgensen, P.B.E. Sandersen, A. Viezzoli, and I. Møller. 2015. 3D geological modelling of a complex buried-valley network delineated from borehole and AEM data. *J. Appl. Geophys.* 122:94–102. doi:10.1016/j.jappgeo.2015.09.004
- Knight, R., R. Smith, T. Asch, J. Abraham, J. Cannia, A. Viezzoli, et al. 2018. Mapping aquifer systems with airborne electromagnetics in the Central Valley of California. *Groundwater* 56:893–908. doi:10.1111/gwat.12656
- Lawrie, K.C., R.S. Brodie, P. Dillon, K.P. Tan, D. Gibson, J. Magee, et al. 2012. BHMAR Project: Assessment of conjunctive water supply options involving Managed Aquifer Recharge options at Menindee Lakes. *Geoscience Australia, Canberra, Australia.*
- Luxem, K. 2017. Managed aquifer recharge in California. *Am. Geosci. Inst., Alexandria, VA.* <https://www.americangeosciences.org/critical-issues/case-study/managed-aquifer-recharge-california> (accessed 2 May 2018).
- Maliva, R.G., R. Herrmann, K. Coulibaly, and W. Guo. 2015. Advanced aquifer characterization for optimization of managed aquifer recharge. *Environ. Earth Sci.* 73:7759–7767. doi:10.1007/s12665-014-3167-z
- Mawer, C., A. Parsekian, A. Pidlisecky, and R. Knight. 2016. Characterizing heterogeneity in infiltration rates during managed aquifer recharge. *Groundwater* 54:818–829. doi:10.1111/gwat.12423
- Minsley, B., J. Ajo-Franklin, A. Mukhopadhyay, and F.D. Morgan. 2011. Hydrogeophysical methods for analyzing aquifer storage and recovery systems. *Groundwater* 49:250–269. doi:10.1111/j.1745-6584.2010.00676.x
- Nenna, V., A. Pidlisecky, and R. Knight. 2011. Application of an extended Kalman filter approach to inversion of time-lapse electrical resistivity imaging data for monitoring recharge. *Water Resour. Res.* 47:W10525. doi:10.1029/2010WR010120
- O'Geen, A., M. Saal, H. Dahlke, D. Doll, R. Elkins, A. Fulton, et al. 2015. Soil suitability index identifies potential areas for groundwater banking on agricultural lands. *Calif. Agric.* 69(2):75–84. doi:10.3733/ca.v069n02p75
- Palacky, G. 1988. Resistivity characteristics of geologic targets. In: M.N. Nabighian, editor, *Electromagnetic methods in applied geophysics.* Soc. Explor. Geophys., Tulsa, OK. p. 52–129. doi:10.1190/1.9781560802631.ch3
- Parsekian, A.D., J. Regnery, A.D. Wing, R. Knight, and J.E. Drewes. 2014. Geophysical and hydrochemical identification of flow paths with implications for water quality at an ARR site. *Groundwater Monit. Rem.* 34:105–116. doi:10.1111/gwmmr.12071
- Pedersen, J.B., F.W. Schaars, A.V. Christiansen, N. Foged, C. Schamper, H. Rolf, et al. 2017. Mapping the fresh-saltwater interface in the coastal zone using high-resolution airborne electromagnetics. *First Break* 35(8):57–61.
- Pidlisecky, A., and R. Knight. 2011. The use of wavelet analysis to derive infiltration rates from time-lapse one-dimensional resistivity records. *Vadose Zone J.* 10:697–705. doi:10.2136/vzj2010.0049
- Pool, D.R., and W. Schmidt. 1997. Measurement of ground-water storage change and specific yield using the temporal-gravity method near Rillito Creek, Tucson, Arizona. *Water-Resour. Invest. Rep.* 97-4125. USGS, Tucson, AZ.
- Strobach, E., B.D. Harris, J.C. Dupuis, A.W. Kopic, and M.W. Martin. 2010. GPR for large-scale estimation of groundwater recharge distribution. In: *Proceedings of the XIII International Conference on Ground Penetrating Radar, Lecce, Italy.* 21–25 June 2010. Curran Assoc., Red Hook, NY. doi:10.1109/ICGPR.2010.5550189
- Viezzoli, A., A. Christiansen, E. Auken, and K. Sørensen. 2008. Quasi-3D modeling of airborne TEM data by spatially constrained inversion. *Geophysics* 73(3):F105–F113. doi:10.1190/1.2895521
- Walsh, D.O., E.D. Grunewald, P. Turner, A. Hinnell, and T.P.A. Ferré. 2014. Surface NMR instrumentation and methods for detecting and characterizing water in the vadose zone. *Near Surf. Geophys.* 12:271–284. doi:10.3997/1873-0604.2013066